

Downscaling Multispectral Satellite Images Without Colocated High-Resolution Data: A Stochastic Approach Based on Training Images

Fabio Oriani^{ID}, Matthew F. McCabe^{ID}, and Gregoire Mariethoz^{ID}

Abstract—Very high-resolution satellite imagery from the latest generation commercial platforms provides an unprecedented capacity for imaging the Earth with very high spatial detail. However, these data are generally expensive, particularly if large areas or temporal sequences are required. In recent years, lower quality imagery has been enabled through the launch of constellations of small satellites with short revisit time. In this article, we apply for the first time a statistical approach to downscale and bias-correct these multispectral satellite data using the information contained in a limited training set of very high-resolution images. The technique, based on the direct sampling algorithm, aims at extending the coverage of high-resolution images by sampling data from a training data set, where similar lower resolution data patterns are found. Unlike the majority of the current downscaling techniques, the approach does not require colocated fine-resolution data, but it is based on the use of training images similar to the target zone. A novel specific setup is proposed, which is adaptive to different types of landscapes with no additional user effort. The results show that the proposed technique can generate more realistic images than the traditional approaches based on the parametric bias correction and bicubic interpolation. In particular, properties such as the intensity histogram, spatial correlation, and connectivity are accurately preserved. The proposed approach can be used to extend the footprint of the high-resolution images to generate new time frames or to downscale the remote sensing imagery based on a distant but structurally similar training image.

Index Terms—Downscaling, machine learning, missing data, multiple-point statistics (MPS), multispectral images, very high resolution.

I. INTRODUCTION

MONITORING and quantification of the earth surface processes rely heavily on the use of satellite imagery, as it offers detailed information on the state and evolution of both environmental phenomena and human activity. The last few decades have seen a significant increase in the number

Manuscript received April 4, 2020; revised June 23, 2020; accepted June 29, 2020. Matthew F. McCabe was supported in part by the King Abdullah University of Science and Technology and in part by the Planet Ambassadors Program. (*Corresponding author: Fabio Oriani*)

Fabio Oriani and Gregoire Mariethoz are with the Faculty of Geosciences and Environment, University of Lausanne, CH-1015 Lausanne, Switzerland (e-mail: fabio.oriani@protonmail.com).

Matthew F. McCabe is with the Hydrology, Agriculture and Land Observation Laboratory, Water Desalination and Reuse Center, King Abdullah University of Science and Technology, Thuwal 23955, Saudi Arabia.

Color versions of one or more of the figures in this article are available online at <http://ieeexplore.ieee.org>.

Digital Object Identifier 10.1109/TGRS.2020.3008015

of spaceborne remote sensing platforms capable of providing a multiband imagery. Projects such as IKONOS, QuickBird, OrbView, Cartosat, and WorldView offer panchromatic and multispectral images with metric to submetric resolution, allowing the precise quantification of object shape and position. These products find application in monitoring the urban activities and infrastructures [1], [2], natural resources and land cover [3], [4], or to quantify damages due to natural disasters [5], [6]. Other applications vary from dynamic cartography to national security [7], as well as oil and gas pipeline monitoring [8] and protection of ecosystems [9]. These images, usually purchased as a single acquisition over a defined area of interest, remain very expensive (potentially thousands of dollars per scene) and limited in both space and time, having a swath width of 10–20 km and often lacking a temporal record (i.e., imagery is captured on-demand rather than as time series). For studies that require continuous data over a large area or long duration, such data are less than ideal. Meanwhile, there are freely available satellite products with high temporal frequencies and global coverage, but with a commensurate reduction in resolution and quality, e.g., platforms launched by national space agencies, such as Landsat-8 or Sentinel-2. More recently, there has also been the addition of comparatively low-cost options provided by the commercial sector, such as the constellation of CubeSats offered by Planet [10], [11].

Developing techniques that combine the spatial accuracy of the very high-resolution (but temporally sparse) images with the denser temporal and spatial coverages of the lower resolution platforms represent an area of appealing research, benefiting from the best of both product types. Indeed, a range of approaches have been proposed to satisfy the need for extending the high-resolution (hi-res) data by generating these images from the correlated products. On popular platforms (e.g., Sentinel, <https://earth.esa.int/web/sentinel>, and Landsat, <https://www.usgs.gov/land-resources/nli/Landsat>), multiple bands are often acquired simultaneously, but at different resolutions. Geostatistical approaches, regression models, or artificial neural networks have all been used in this context to downscale the coarser scale bands to the resolution of a fine-scale predictor [12]–[15]. A particular example of a geostatistical technique that has been successfully deployed in the downscaling applications is the area-to-point cokriging (ATPCK) [16], as well as its variants, such as the combined use of ATPCK and multiple-point statistics (MPS) [17].

Data-fusion procedures usually require an important component related to the bias correction of the input or output images: this is required, since the predictor images are generated using different sensors or in different light conditions. This results in homogeneous or variable intensity bias. The approaches to overcome this problem are mainly based on regression [18], [19] or histogram transformation [20] and can be mediated by image classification to accommodate nonstationarity [19], [20].

Covariates have also been used as hi-res predictors in the downscaling procedure. Taking the example of thermal remote sensing, land surface temperature has been estimated using regression kriging [21] or based on the empirical relationships involving vegetation and soil indices [22]–[25], and heat islands have been quantified with regressions against other sensors [26]. Similar techniques are used to derive other variables, such as bias-corrected precipitation estimation using ground data [27] and environmental parameters such as vegetation, albedo, drought index, and topography [28], [29], or to estimate the hi-res soil moisture data [30]–[32], including the analysis of spectral features [33]. More complex approaches to the downscaling of the satellite-derived precipitation and soil moisture data include artificial neural network models [34]–[36]. All these approaches require that hi-res information is available on the target footprint of the image as a predictor variable, yet such information is not always present in practice. When the local hi-res information is not available for a large area or time span, the fine-scale features cannot be determined.

The purpose of this contribution is to consider such cases and to explore the generation of hi-res variables by stochastic generation. We propose a stochastic simulation technique relying on a training data set and the colocated satellite images at lower resolution (about one-third of the target resolution in the cases studied in this article). Importantly, this technique does not require the colocated hi-res information, but instead relies on a hi-res training image (TI) from a nearby area, an area showing similar landscape features, or a past snapshot of the same area. The proposed approach is based on the direct-sampling (DS) algorithm [37], which uses a multivariate data set as TI. DS requires the formulation of a specific setup according to the kind of application: this includes the choice of conditioning or cosimulated variables and the simulation parameters. DS has been previously used to simulate the missing portions of the satellite data [38], for the simulation of the radar-derived rainfall fields conditioned by elevation and weather state [39], or to downscale 50- to 10-km precipitation and temperature fields generated using the Weather Research and Forecasting (WRF) model [40]. These works indicate that DS is a good candidate to simulate realistic spatial patterns that preserve the higher order statistics characterizing natural structures.

In the proposed application, the TI contains coregistered images at a lower (3 m) and a higher (1 m) resolution, but from an adjacent zone or another area showing similar geographical features as the region of interest. The TI contains data patterns that represent the statistical association between the lower and higher resolution heterogeneities, and it is used as the source of information to downscale a given low-resolution

(lo-res) image. The algorithm retrieves a lower resolution data pattern from the region of interest and generates higher resolution data by sampling the TI where a similar pattern occurs. Relying uniquely on pattern generation, this strategy avoids the explicit formulation of a statistical model. More importantly, no colocated hi-res images or predictive variables for the target zone are necessary.

In this article, we apply the technique for the first time to the downscaling of the multispectral satellite imagery, showing highly complex heterogeneity at both large and small scales, related to natural and anthropogenic structures. The proposed framework includes the use of a k -means unsupervised classification of the lo-res image, which is also used as an auxiliary variable. We also propose a specific parameter setup to account for the resolution jump between the conditioning and simulated data. The technique is tested on different case studies: a forested landscape in Botswana, a tide-dominated shoreline area in Port Hedland (Western Australia), and the urban area of Alice Springs (Northern Territory, Australia). For this last study area, the approach is tested using two types of TIs: an adjacent urban zone and a similar landscape from a distant region. The latter case represents an example where the chosen TI is suboptimal, because it does not present a close match with the target zone regarding the intensity histogram. The article is organized as follows. Section II illustrates the downscaling technique, Section III presents the data set used and the numerical test performed, while the results are shown in Section IV and discussed in Section V. Section VI is dedicated to the conclusions.

II. METHODOLOGY

A. DS Technique

DS [37] is a geostatistical simulation technique belonging to the family of MPS [41], [42]. MPS is based on the use of a TI, containing data (or a conceptual representation of the heterogeneity) to simulate, and a simulation grid (SG), used to host the simulated data and the given conditional data, if present. In general, the TI is used to estimate the probability of occurrence of a certain value in a location of the SG given the conditional, or the already simulated, data in its neighborhood. In this way, the MPS algorithm can simulate the random values, while preserving the complexity of data patterns in space.

DS differs from previous MPS techniques mainly by short-cutting the simulation phase. Instead of estimating the conditional probabilities, the algorithm retrieves the neighborhood data pattern from the SG and samples data from the TI, where a similar pattern is found. Therefore, instead of sampling from a conditional probability distribution, DS directly samples the data set that would have been used to estimate that distribution.

In the following, we describe the main workflow of the DS algorithm (for further details, see the DeeSse 2017 documentation, www.randlab.org).

- 1) Select a random location x in the SG that has not yet been simulated.
- 2) To simulate a variable $Z(x)$ (e.g., an image pixel at the location x), retrieve the data event $\vec{d}(x)$, which consists

of the N closest data neighbors of x within a radius corresponding to 1/4 of the TI size.

- 3) Visit a random location y in the TI and retrieve the corresponding data event $\vec{d}(y)$.
- 4) Compute a distance $D(\vec{d}(x), \vec{d}(y))$, i.e., a measure of dissimilarity between the two data events. For categorical variables, the proportion of nonmatching elements in $\vec{d}(\cdot)$ is used as a criterion

$$D(\vec{d}(x), \vec{d}(y)) = N^{-1} \sum_{n=1}^N \mathbb{I}_{d_n(x) \neq d_n(y)} \quad (1)$$

where $d_i(\cdot)$ is the n th datum composing the conditioning pattern. While for continuous variables, we use the mean absolute error

$$D(\vec{d}(x), \vec{d}(y)) = N^{-1} \sum_{n=1}^N |d_n(x) - d_n(y)|. \quad (2)$$

- 5) If $D(\vec{d}(x), \vec{d}(y))$ is smaller than a fixed threshold T , assign the value of $Z(y)$ to $Z(x)$. Otherwise, repeat from steps 3 to 5. T is expressed as a fraction of the range of Z in the TI. For example, $T = 0.05$ allows $D(\vec{d}(x), \vec{d}(y))$ up to 5% of the total variation observed in the TI. For categorical variables, $T = 0.05$ allows a mismatch between $\vec{d}(x)$ and $\vec{d}(y)$ for 5% of the neighbors.
- 6) If a prescribed TI fraction F is covered by the scan, assign to $Z(x)$ the scanned datum $Z(y^*)$ that minimizes D among the visited candidates.
- 7) Repeat the whole procedure for all uninformed locations in the SG.

The algorithm relies, therefore, on the following parameters: the maximum scanned TI fraction $F \in (0, 1]$, the maximum number of neighbors N , both expressed in the number of pixels, and the distance threshold $T \in (0, 1]$. Importantly for the present application, DS can be applied to the multivariate case, where a stack of colocated variables are simulated together by considering the multivariate data patterns as a unique data event. Apart from F , the parameters can be set separately for each simulated variable, allowing different size for the conditioning data patterns and distance threshold. According to the previous applications and sensitivity analysis [43]–[45], the setup, empirical and related to the size of characteristic structures and their complexity, can be manually established and kept constant for a specific application type, being usually adaptive to different data sets. Section II-B presents a specific setup for the proposed application that is kept constant over different study cases.

B. Generic Simulation Framework for Multiband Image Downscaling

For the application considered in this article, a multivariate DS setup is necessary, where the hi-res variables are simulated together following the workflow described in Section II-A. The goal is to formulate a generic simulation framework for multiband satellite image downscaling that can be adaptive to different earth surface types. In order to do this, we rely only on the satellite images as the source of information, without external data.

TABLE I
STANDARD SETUP PROPOSED FOR MULTIBAND SATELLITE IMAGE DOWNSCALING. THE PARAMETERS ARE: MAXIMUM NUMBER OF CONDITIONING NEIGHBORS N AND DISTANCE THRESHOLD T .
THE VARIABLES ARE: 1) LO-RES k -MEANS CLASSIFICATION (K_L), 2)–5) R, G, B, AND NIR LO-RES IMAGES (L_R , L_G , L_B , AND L_{NIR}), AND 6)–9) R, G, B, AND NIR HI-RES IMAGES (H_R , H_G , H_B , AND H_{NIR})

Variable	description	N	T	simulated/given
1) K_L	k -means on lo-res bands, $k=5$	240	0.01	given
2) L_R	lo-res red	10	0.005	given
3) L_G	lo-res green	10	0.005	given
4) L_B	lo-res blue	10	0.005	given
5) L_{NIR}	lo-res near-infrared	10	0.005	given
6) H_R	hi-res red	10	0.005	simulated
7) H_G	hi-res green	10	0.005	simulated
8) H_B	hi-res blue	10	0.005	simulated
9) H_{NIR}	hi-res near-infrared	10	0.005	simulated

The DS setup proposed (Table I) consists in using as TI a lo-res multiband image (L_R , L_G , L_B , and L_{NIR}) together with a hi-res colocated image (H_R , H_G , H_B , and H_{NIR}) for an area that shows a similar terrain as the target region of downscaling. In the target area, only lo-res data are available (L_R , L_G , L_B , and L_{NIR}). For example, TI and SG can correspond to different zones in a geographically uniform region, or they can be exactly colocated in space but taken at different time intervals. The TI has all variables informed, while the SG hosts the lo-res bands as the conditioning data and all the hi-res bands are simulated together. For these variables, we set up by trial and error the parameters $N = 10$ and $T = 0.005$, in agreement with the values previously used in multivariate spatial simulation [39]. To make the TI more compatible with the target region, a quantile transformation can be applied to the lo-res bands of the TI to match exactly the histogram of the lo-res bands in the target region. This has been the case for the fourth test presented in this article (Section IV-B).

In addition to the raw image bands, we add an auxiliary variable K_L , the k -means classification [46] computed on the joint lo-res bands. K_L allows for the identification of nonstationarity in the image and to distinguish different types of objects if visible at the low-resolution. It is used as a covariate with a larger number of neighbors ($N = 240$) and distance threshold ($T = 0.01$) to provide general information on the position and type of the data patterns. For the k -means classification, we have chosen $k = 5$, as it is generally sufficient to describe different types of landscapes.

III. TESTING AND VALIDATION

A. Presentation of the Test Data Sets

The data used in this study consist of a set of four-band—red (R), green (G), blue (B), and near-infrared (NIR)—satellite images by Planet (www.planet.com). Although presenting a rather high (3 m) resolution, these images are used in this study as a starting “lo-res” product to downscale. The main limitation of these products resides in the accuracy, since they present known biases due to the low-cost nature of the

sensors used [47]. The hi-res counterpart, used to train and validate the model, is a set of four-band (R, G, B, and NIR) images from the WorldView-3 and -4 commercial satellites by DigitalGlobe (www.digitalglobe.com), with a resolution of 1.24 m. All images used in this study are exempt of clouds. We consider three regions to test the proposed technique: a forested area of about 3.2 km² in Botswana, a 1.8-km² urban district of Alice Springs (Northern Territory), and an 8.5-km² tide-dominated coastal area near Port Hedland (Western Australia). Hereon, these cases are labeled “Botswana,” “Alice Springs,” and “Port Hedland.” As the fourth case study “Alice Springs-2,” a larger portion of the Alice Springs urban district (1.8 km²) is considered as the study zone, using the urban area of South Hedland (Western Australia) as TI (6.3 km²). To keep consistency in the image content, the WorldView (WV) and Planet (Pl) images are taken within a short time interval, with the following timestamps: 11.6.2016 (WV) and 23.7.2016 (Pl) for Botswana; 19.05.2017 (WV) and 22.05.2017 (Pl) for Alice Springs and Alice Springs-2; and 21.6.2017 (WV) and 18.6.2017 (Pl) for Port Hedland and South Hedland.

The WorldView image of Alice Springs has been orthorectified to compensate for the distortion linked to the perspective view of the sensor and the relief (the product can be purchased already orthorectified). The NASA’s Shuttle Radar Topography Mission (SRTM, www2.jpl.nasa.gov/srtm/) digital elevation model with the open-source software Orfeo Toolbox (www.orfeo-toolbox.org) have been used for this purpose.

Fig. 1 shows an overview of the regions used in the downscaling exercises: for the first three case studies, the downscaling is applied to approximately one-third of each image (red rectangle indicating the SG), while the remaining part is used as TI. For Alice Springs-2, the training [Fig. 1(d)] and target [Fig. 1(e)] images belong to two separated images. Recall that according to the simulation framework (Table I), a total of nine colocated variables are considered in both the TI and SG: the lo-res images (L_R , L_G , L_B , and L_{NIR}) as well as the derived k -means classification (K_L) are informed in both the TI and the SG as conditioning data, while all the hi-res variables (H_R , H_G , H_B , and H_{NIR}) are informed only in the TI and they are simulated in the SG.

B. Comparison With Other Techniques

The proposed methodology based on DS simulation is compared with the common bicubic spline interpolation [48], combined with two different techniques for bias correction, which rely on the analysis of the training data set. The two bias-correction techniques proposed rely, respectively, on linear correlation and histogram transformation, similarly to previous remote sensing applications (see Section I). Following the workflow represented in Fig. 2(a), the hi-res image in the training area is first projected to the lo-res grid to allow the registration of the lo-res image using this image as reference. The adopted registration technique consists of estimating a rigid transformation matrix that maximizes the linear correlation between both images by rotation and translation. More complex image-registration techniques can be used if necessary to achieve an optimal image superposition. Once

performed, a linear regression model is calibrated using all the lo-res bands to predict each hi-res band separately. This relation is used to bias-correct the lo-res image in the target area. The bias-corrected image is then downscaled by applying the bicubic interpolation, leading to the final hi-res image product based on linear regression with Bi-Cubic interpolation (LBC). As an alternative method, the lo-res image of the target area is bias-corrected by applying a quantile–quantile transformation to match the histogram of the hi-res TI projected on the lo-res grid. This relies on the hypothesis of stationarity and similar statistical content between the training and target areas. The obtained image is then downscaled by applying the bicubic interpolation, obtaining a second downscaling product histogram transform with Bi-Cubic interpolation (HBC). HBC and LBC are compared with that obtained using DS. Since DS needs all images defined on the same grid, the lo-res images of both the training and target areas are projected on the hi-res grid using the nearest neighbor interpolation [Fig. 2(b)]. Note that this is just a regridding operation with no downscaling of the heterogeneity involved. The DS algorithm is then applied (see Section II) to simulate the hi-res image of the target area.

C. Validation

The obtained downscaled image products (HBC, LBC, and DS) are first analyzed by visual comparison with the reference and lo-res images of the study areas. A k -means classification is then computed on the downscaled hi-res images to verify how well the technique can preserve particular objects within the landscape. The number of classes (k) is set to 5, which allows the identification of the main objects composing all considered landscapes. The intensity and k -means class histograms of all images are computed to quantify how the statistical content is preserved by downscaling. In addition, the following error indices are computed to evaluate the quality of the generated images: the root-mean-squared error (RMSE) between the reference and downscaled images, and between their histograms and their experimental variograms. The structural similarity index (SSIM) [49] is also computed to compare the quality of the images with respect to the reference. This indicator is based on the match of the average local mean, variance, and covariance computed on a sliding window. In this study, SSIM is the average value computed for a logarithmic series of window sizes from 3×3 to 300×300 pixels, to cover different pattern scales over the study zone. Higher SSIM values indicate more similarity, with a value of 1 in the case of exact match. Moreover, the k -means classification of the downscaled images is compared with that of the reference using the following indicators: the fraction of pixels presenting a nonmatching class (k -means miss fraction), separated into the underestimation of the class coverage (miss by disagreement) and wrong spatial distribution of the class (miss by location). The topology of the different classes is analyzed with a connectivity indicator [50] measuring the probability, defined in [0,1], of the two pixels of the same classes being connected through a continuous path. The resulting value is the RMSE between the reference and downscaled connectivity of all k -means classes.

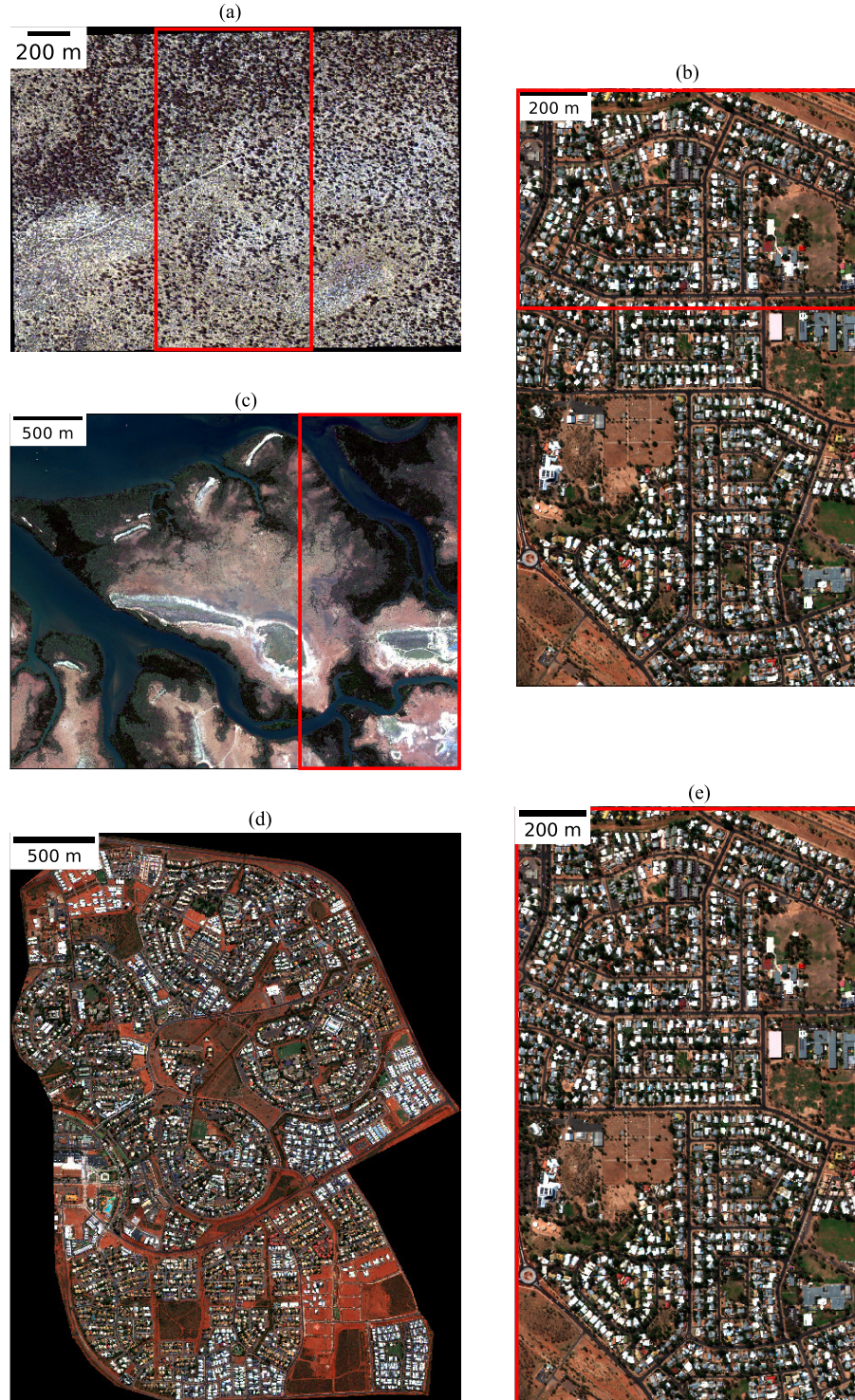


Fig. 1. Overview of the hi-res RGB images for the considered case studies. (a) Botswana, (b) Alice Springs, and (c) Port Hedland. The red rectangle indicates the area which is downsampled (SG) and for which the hi-res product is used as reference, while the rest of the image is used to train the algorithm (TI). For the fourth study case, the urban area of (d) South Hedland is used as TI while (e) Alice Springs is used as target image.

IV. RESULTS

A. Test Cases With Optimal TIs

The first case study (Botswana, Fig. 3) presents a sparsely forested area covered by a varying density of trees. This is visible in the lo-res image as well as in its k -means

classification [Fig. 3(a) and (b)]. Patches of trees close to each other and associated with a darker terrain are identified by the dark blue class, which gradually transitions to the clearings identified by the yellow class. The hi-res ref image [Fig. 3(i) and (j)] adds significant detail, revealing individual trees as well as the presence of a road. The image downsampled

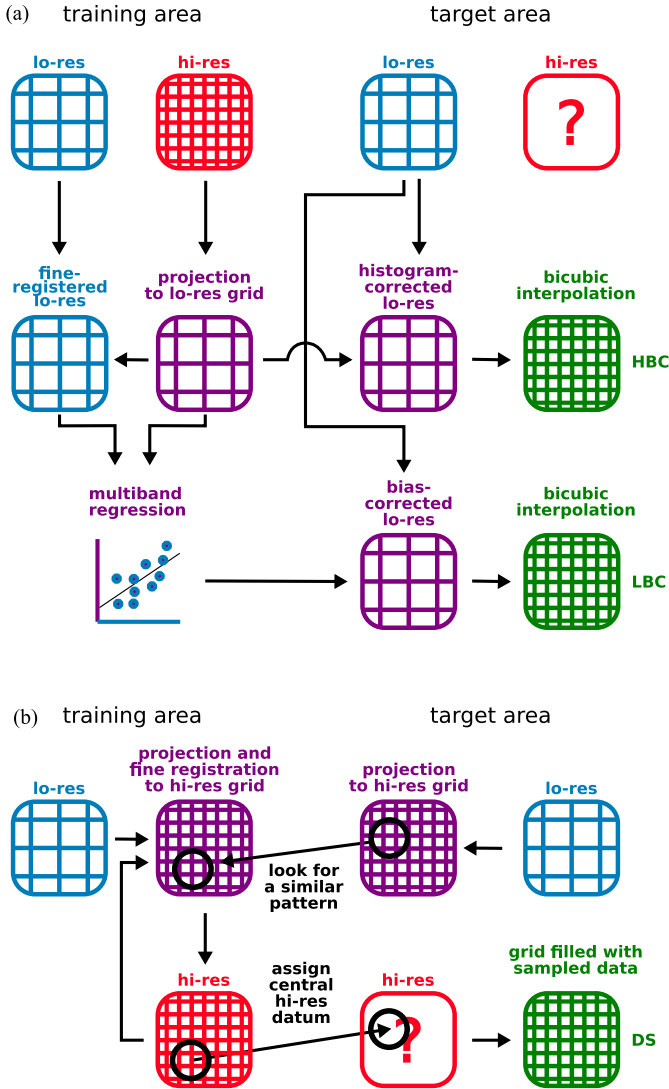


Fig. 2. Schematic of the downscaling workflows compared. (a) HBC/LBC and (b) DS. Grids represent different types of images: blue for lo-res, red for hi-res, purple for intermediate products, and green for final products. The output images are based on histogram transformation and bicubic interpolation for HBC, linear regression and bicubic interpolation for LBC, and pattern-based resampling for DS.

using the techniques HBC and LBC [Fig. 3(c) and (f)] does not add significant details to the landscape, but HBC presents a color distribution more similar to the hi-res reference (i). Conversely, the image generated using DS [Fig. 3(g) and (h)] shows a spatial distribution of the trees similar to the reference: the density and irregular geometry of the patches are fairly well preserved, although with a moderate underestimation of the small elements. There is a moderate loss in the variability of the large-scale terrain color distribution, which looks too homogeneous in the simulation, while the road is completely absent. From the image subset (Fig. 4), it is visible that the output of DS downscaling preserves the small-scale heterogeneity with a realistic detail and a minimal amount of added noise [Fig. 3(g) and (h)]: individual trees are correctly classified as the *k*-means blue class, associated with their respective shadows. The small-scale geometry in the spatial

distribution of both types of soils is also preserved (green-to-yellow classes). Fig. 5 shows that the reference histogram of the lo-res image [Fig. 5(a) and (b)] differs significantly from its hi-res counterpart [Fig. 5(i) and (j)]. Such a discrepancy indicates a significant bias of the Planet images compared with the WorldView imagery. HBC corrects in part this histogram bias [Fig. 5(c)], while LBC does not show a similar improvement. The DS simulation presents the closest histogram to the reference. All images have a similar *k*-means histogram (Fig. 5, right column).

The case study of Alice Springs (Fig. 6) presents a more complex heterogeneity, featuring diverse buildings aggregated in various configurations, with city blocks varying in orientation and shape. This landscape also includes open areas with sporadic tree coverage, along with an irregular road network. The lo-res image and its classification [Fig. 6(a) and (b)] provide a broad detection of these elements, although their shape is not well represented. The reference hi-res image [Fig. 6(i) and (j)] brings more geometric details and allows one to distinguish roofs from the nearby trees, as well as the continuity of roads. HBC [Fig. 6(c) and (d)] and LBC [Fig. 6(e) and (f)], similar to the previous case, do not add significant details to the downscaled image; conversely, HBC presents a smoother *k*-means classification. The DS simulation [Fig. 6(g) and (h)] presents small-scale noise but offers a sharper representation of the elements than the lo-res image. The zoomed-in area (Fig. 7) shows that, although not reaching the accuracy of the real hi-res image, DS [Fig. 7(g) and (h)] preserves the surface occupied by buildings and vegetation, approaching the true color and geometry. Some small-scale elements, particularly underrepresented in the TI, are completely missing from the simulation, e.g., the red roof and sports fields [Fig. 7(i)]. Likewise, the continuity of the road network is not always preserved, but, compared with HBC and LBC [Fig. 7(d) and (f)], the *k*-means classification of DS [Fig. 7(h)] is much more similar to the reference image. Again, the intensity histogram and the *k*-means classes distribution are accurately preserved in the DS simulation [Fig. 8(g) and (h)], correcting the bias present in the lo-res image [Fig. 8(a)]. The histograms also show that the TI [Fig. 8(k)] is the representative of the target region of interest [Fig. 8(i)]. While not accurately representing the spatial patterns of the reference, HBC shows a similar performance as DS in terms of preserving both the multiband histogram [Fig. 8(c)] and distribution of classes [Fig. 8(d)].

The third case study (Port Hedland, Fig. 9) comprises a semiarid tide-dominated coastal region, with distinctive subenvironments: meandering channels with mangrove vegetation lie adjacent to a drier intertidal zone, featuring salt deposits and partially vegetated sand bars. The area is approximately twice as large as the previous examples, and includes complex small-scale structures in the subenvironment transition zones, as well as oriented structures. The large-scale variability is captured by the lo-res image [Fig. 9(a) and (b)], while the hi-res reference image [Fig. 9(i) and (j)] adds details on the spatial distribution of the vegetation and land-cover types. HBC [Fig. 9(c) and (d)] presents an overall distribution of colors visually more similar to the hi-res reference, but also leads

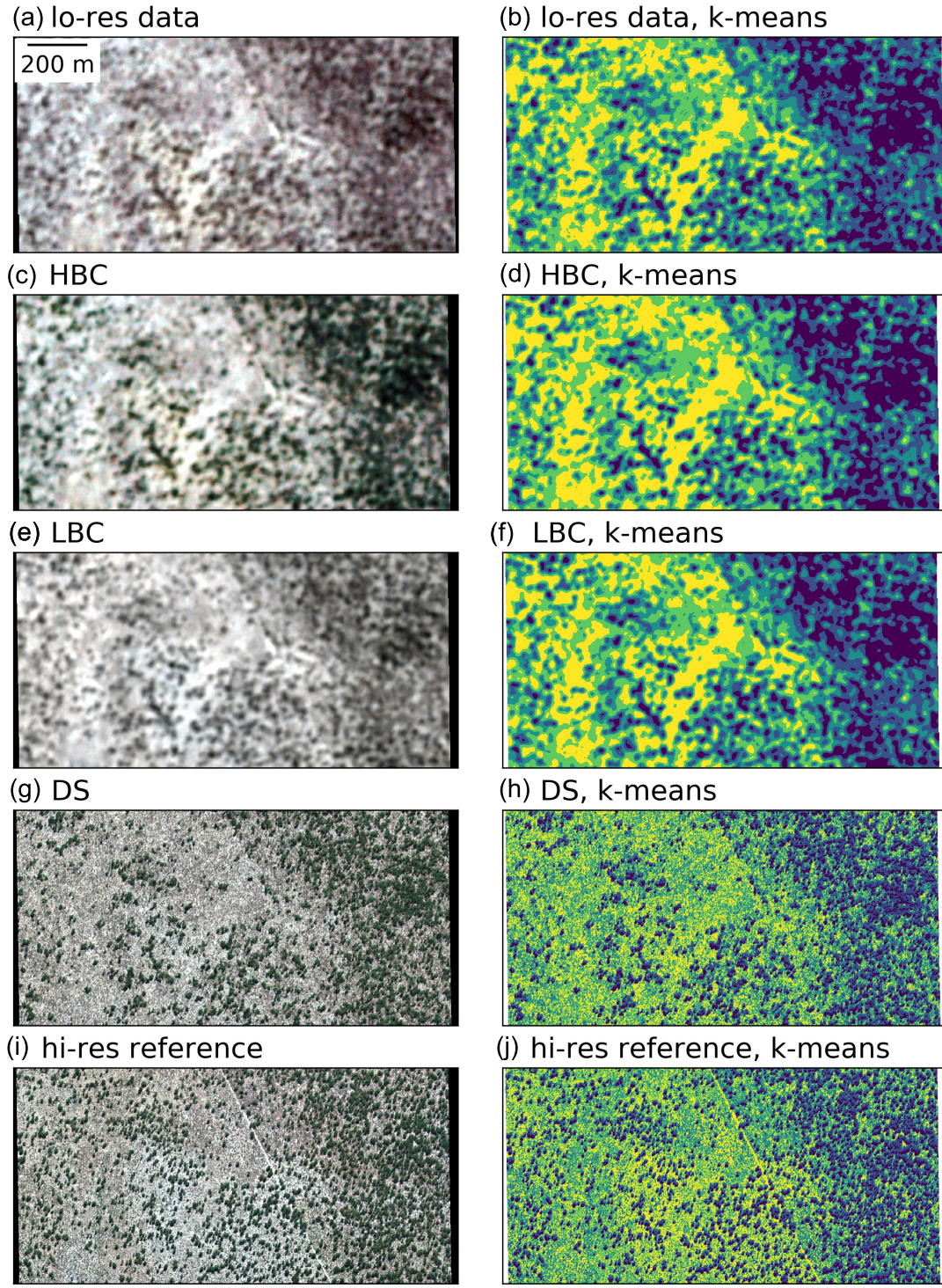


Fig. 3. Visual comparison among RGB images and k -means classification for the Botswana case study. (a) and (b) Lo-res input image. Image downscaled using (c) and (d) HBC, (e) and (f) LBC, and (g) and (h) DS. (i) and (j) Reference hi-res image.

to a misclassification of some inland areas that have the class used for water (dark blue). LBC [Fig. 9(e) and (f)] presents a visually biased color distribution and a smooth but overall more correct classification. Similar to the previous cases, DS [Fig. 9(g) and (h)] represents the hi-res color distribution and classification with more accuracy. Small-scale features such as the gradual transition from the vegetated coastal areas

to inland clearings are reconstructed with realistic details. Some blue-shaded terrains present in the top border of the region, possibly linked to salt deposits, are generally absent in the TI, and thus not preserved in the simulation. The zoomed-in position (Fig. 10) shows that the meandering structure of the channels and the complex distribution of vegetation are more detailed in the DS simulation [Fig. 10(g) and (h)] with

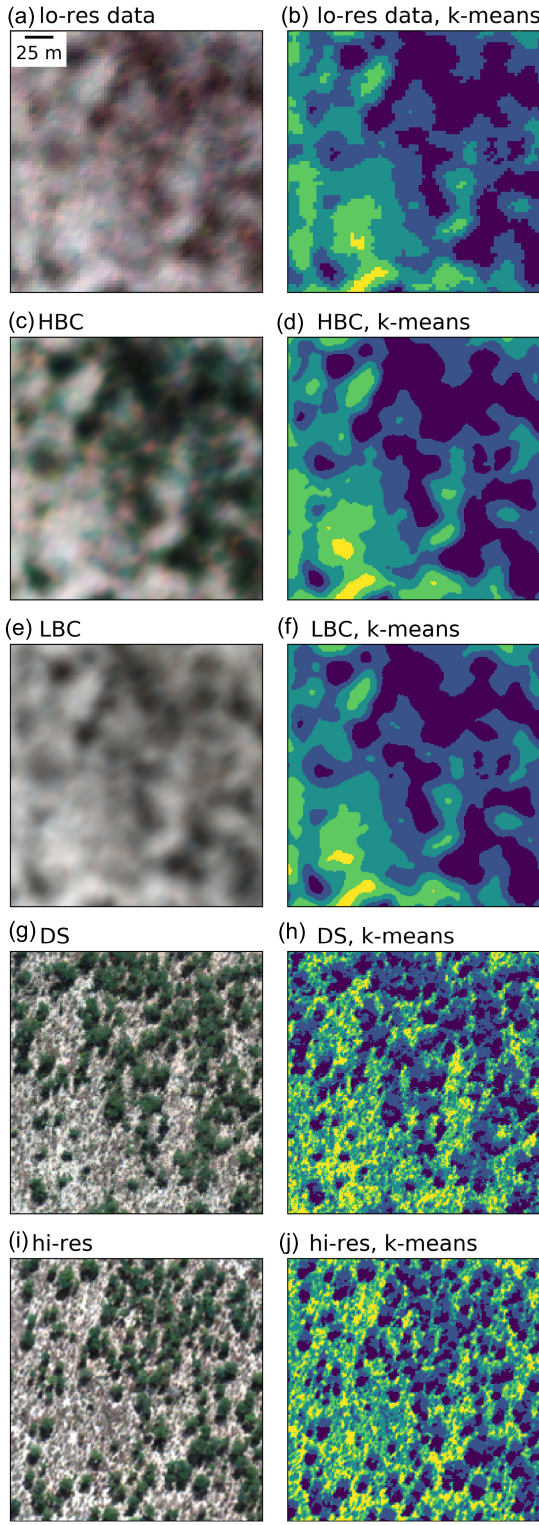


Fig. 4. Details from the Botswana case study, showing a visual comparison among the RGB images and *k*-means classification. (a) and (b) Lo-res input image. Image downsampled using (c) and (d) HBC, (e) and (f) LBC, and (g) and (h) DS. (i) and (j) Reference hi-res image.

respect to HBC [Fig. 10(c) and (d)] and LBC [Fig. 10(e) and (f)], although the continuity of small inlets is not entirely preserved. Fig. 11 shows that the biases in the intensity histogram are corrected with the downscaling procedure of DS [Fig. 11(g)], while HBC [Fig. 11(c)] and

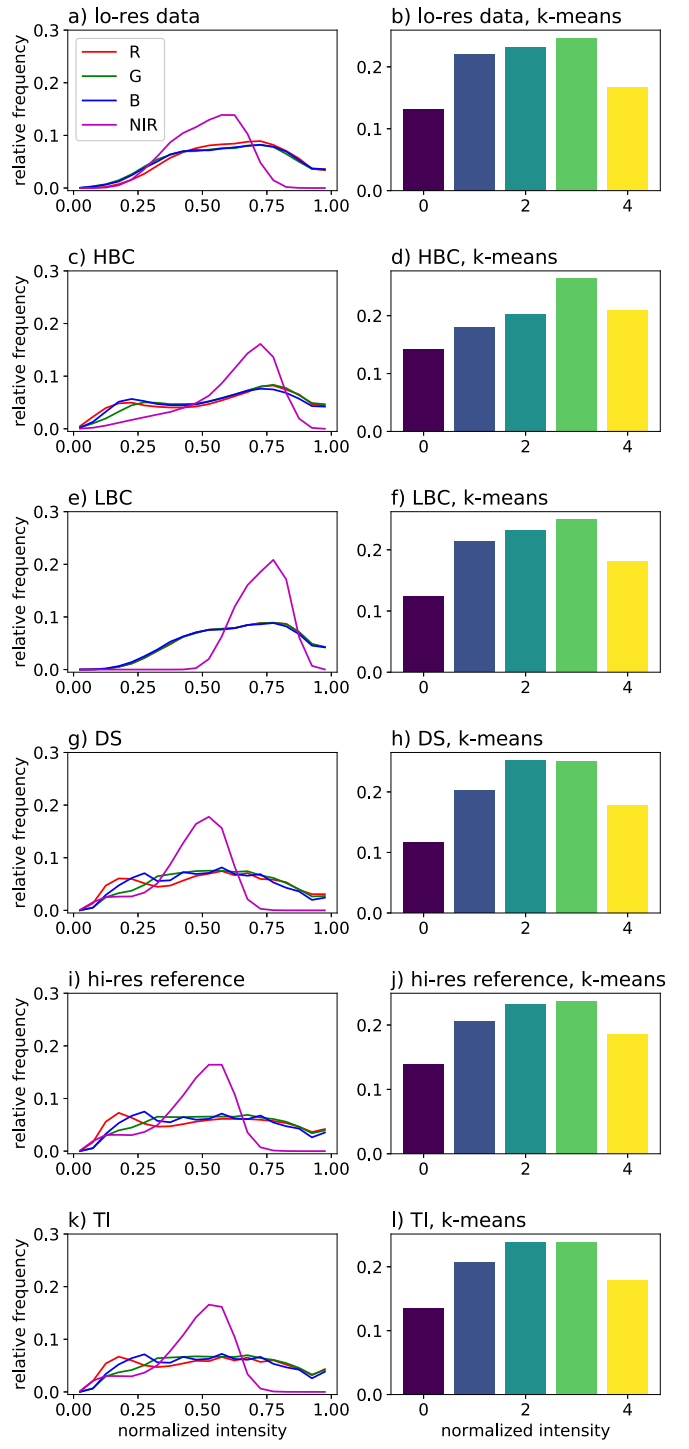


Fig. 5. Histograms for the Botswana case study of the R, G, B, and NIR bands and *k*-means classification. (a) and (b) Lo-res conditioning data. Image downsampled using (c) and (d) HBC, (e) and (f) LBC, and (g) and (h) DS. (i) and (j) Hi-res reference. (k) and (l) TI. The bin colors for the *k*-means histograms match the class colors in Fig. 3.

LBC [Fig. 11(e)] cannot approach the same intensity distribution. In particular, the HBC bias correction is influenced by the training data set [Fig. 11(k)], which shows a moderate discrepancy with respect to the reference [Fig. 11(i)]. DS also presents a more accurate *k*-means histogram [Fig. 10(j)] than the HBC [Fig. 11(d)] and LBC [Fig. 11(f)], with respect to the hi-res reference [Fig. 11(j)].

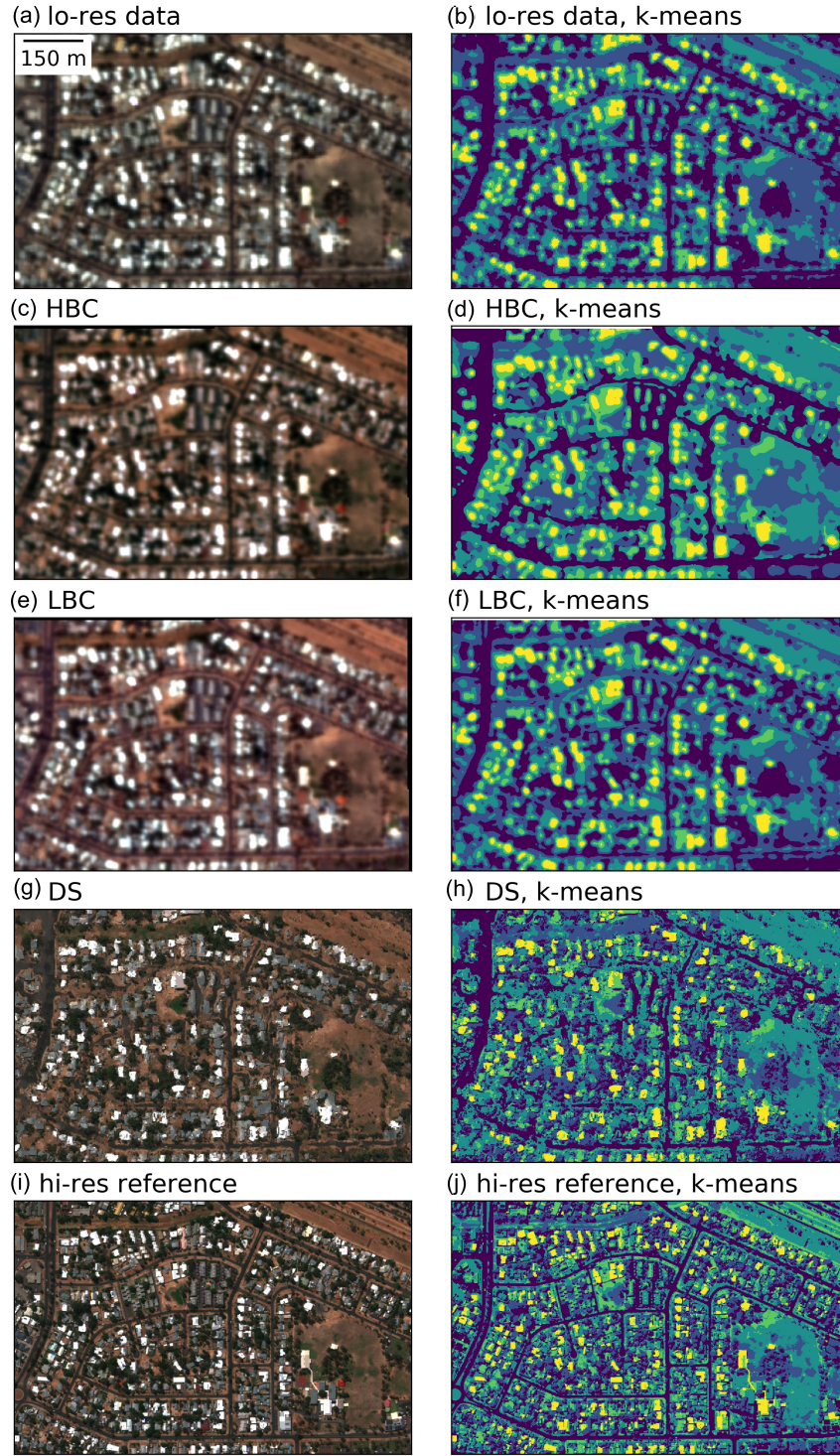


Fig. 6. Visual comparison among the RGB images and k -means classification for the Alice Springs case study. (a) and (b) Lo-res input image. Image downscaled using (c) and (d) HBC, (e) and (f) LBC, and (g) and (h) DS. (i) and (j) Reference hi-res image.

B. Test Case With a Suboptimal TI

The last case study consists of downscaling a larger portion of the Alice Springs urban area. With respect to the previous case study on Alice Springs (Fig. 6), here, a larger area is downscaled and the TI belongs to the Southern Hedland urban area [Fig. 1(d)], a distant region presenting a compatible landscape. As seen in the visual comparison (Figs. 12 and 13),

DS allows again adding more details to the downsampled images with respect to the other considered techniques. The image downsampled with DS presents statistics [Fig. 14(g) and (h)] similar to the ones with the TI [Fig. 14(k) and (l)]. At the same time, these depart more from the reference histograms [Fig. 14(i) and (j)] with respect to the other study cases. HBC shows a comparable result to DS regarding the intensity

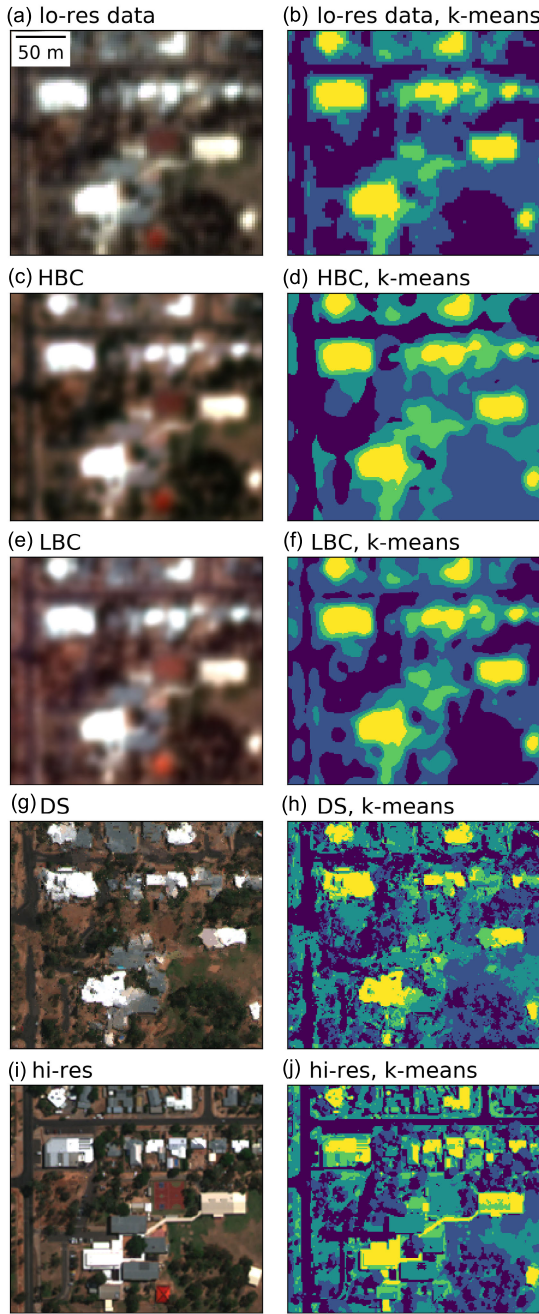


Fig. 7. Details from the Port Hedland case study, showing a visual comparison among the RGB images and k -means classification. (a) and (b) Lo-res input image. Image downsampled using (c) and (d) HBC, (e) and (f) LBC, and (g) and (h) DS. (i) and (j) Reference hi-res image.

histogram [Fig. 14(c)], while LBC shows a worse performance [Fig. 14(e)]. Both HBC and LBC better preserve the class histogram [Fig. 14(d) and (f)] than the DS [Fig. 14(h)].

C. Quantitative Indicators

Table II summarizes the performance of all techniques with a series of quantitative indicators (see Section III-C) for all case studies. For global error measures such as the RMSE on the pixel values or the k -means miss fraction, the three techniques show a comparable performance, with a high miss

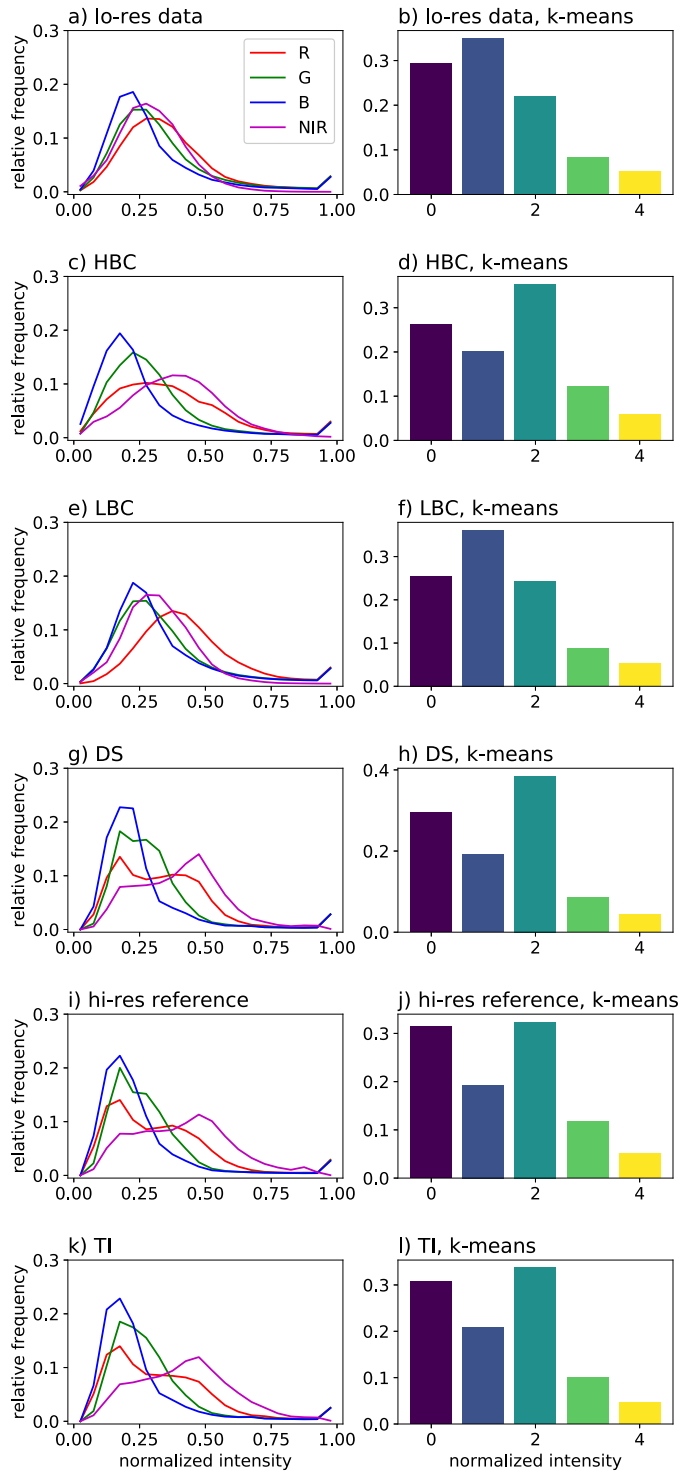


Fig. 8. Histograms for the Alice Springs case study for the R, G, B, and NIR bands and k -means classification. (a) and (b) Lo-res conditioning data. Image downsampled using (c) and (d) HBC, (e) and (f) LBC, and (g) and (h) DS. (i) and (j) Hi-res reference. (k) and (l) TI. The bin colors for the k -means histograms match the class colors in Fig. 6.

fraction (>0.5) that is mainly due to a misplacement of small-scale features for the case studies of Botswana and Alice Springs. HBC and LBC generally present a higher SSIM than DS, meaning that they tend to preserve slightly better local mean, variance, and covariance with the reference at different scales. Nevertheless, the histogram RMSE scores confirm that

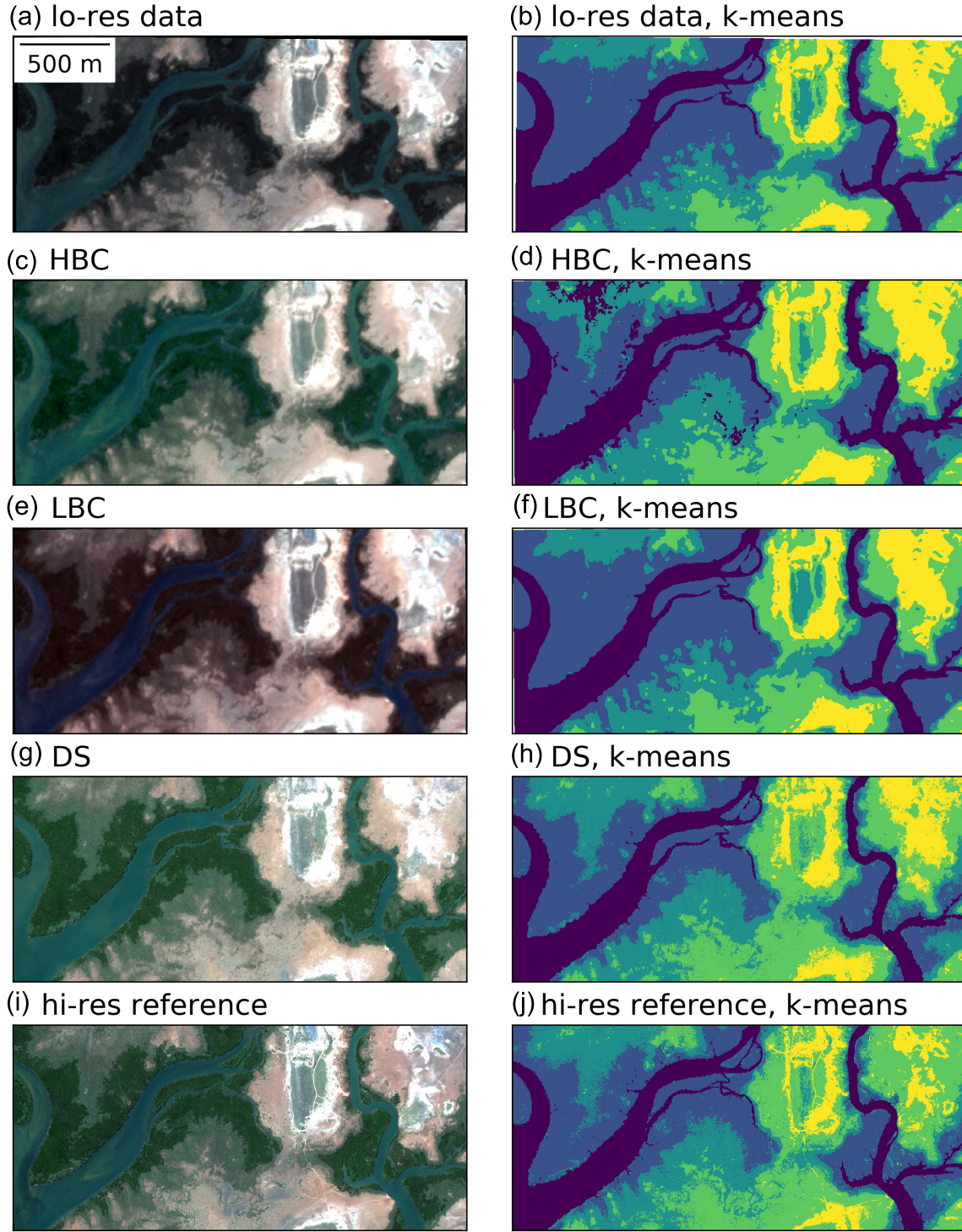


Fig. 9. Visual comparison among the RGB images and the *k*-means classification for the Port Hedland case study. (a) and (b) Lo-res input image. Image downsampled using (c) and (d) HBC, (e) and (f) LBC, and (g) and (h) DS. (i) and (j) Reference hi-res image.

DS better preserves the reference histogram. Regarding the spatial indicators, such as the RMSE of the variogram and *k*-means connectivity, DS presents significantly higher scores for all case studies.

V. DISCUSSION

The case studies examined in this analysis illustrate how the proposed downscaling technique based on the DS algorithm

is able to generate realistic small-scale features approaching those depicted in the hi-res satellite imagery by relying on the use of a TI. Its performance is demonstrated by the lower error shown by DS with respect to HBC and LBC in the variogram and connectivity of the *k*-means classes. This suggests that DS better preserves spatial variations and connectivity of the classified objects. This is an important result considering that no conditional data are given at the hi-res, with the algorithm

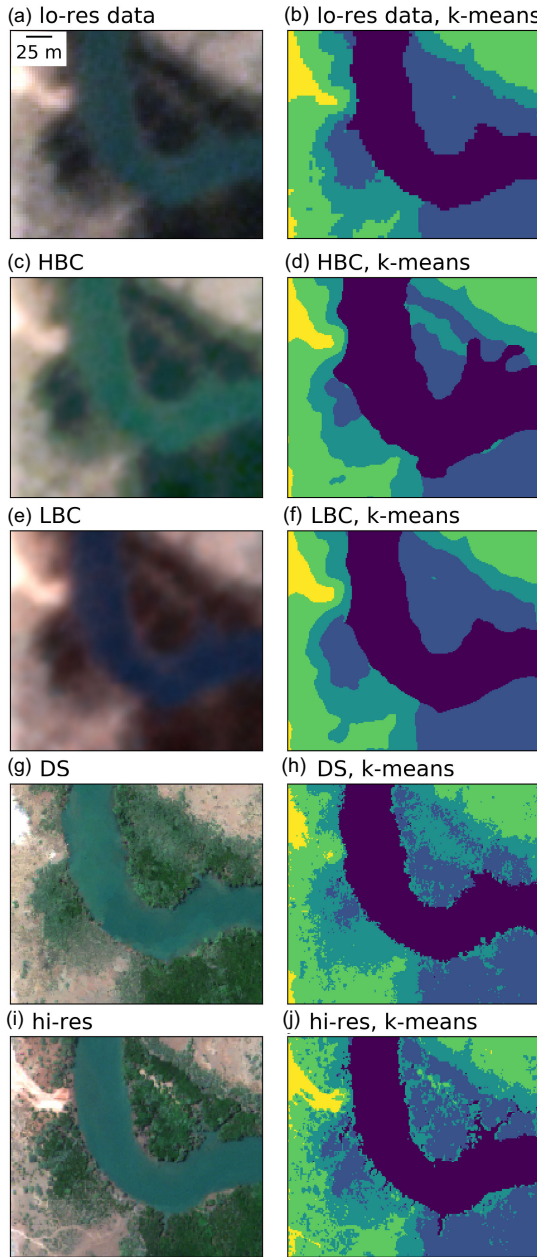


Fig. 10. Details from the Port Hedland case study, showing a visual comparison among RGB images and k -means classification. (a) and (b) Lo-res input image. Image downsampled using (c) and (d) HBC, (e) and (f) LBC, and (g) and (h) DS. (i) and (j) Reference hi-res image.

being based only on the information contained in the TI and guided by the lo-res image. Note that the input k -means classification is derived solely from the lo-res image and the hi-res k -means is used only for validation. HBC can benefit from the histogram transformation to correct the histogram bias. Nevertheless, the results show that in all cases, HBC and LBC do not preserve the reference histograms as accurately as DS. Global error metrics show comparable scores among the different techniques, with sometimes better scores shown by bicubic interpolation. This result is typical of smooth interpolators or linear regressions, since they tend to pass in between the local peaks and, thus, obtain a lower average error

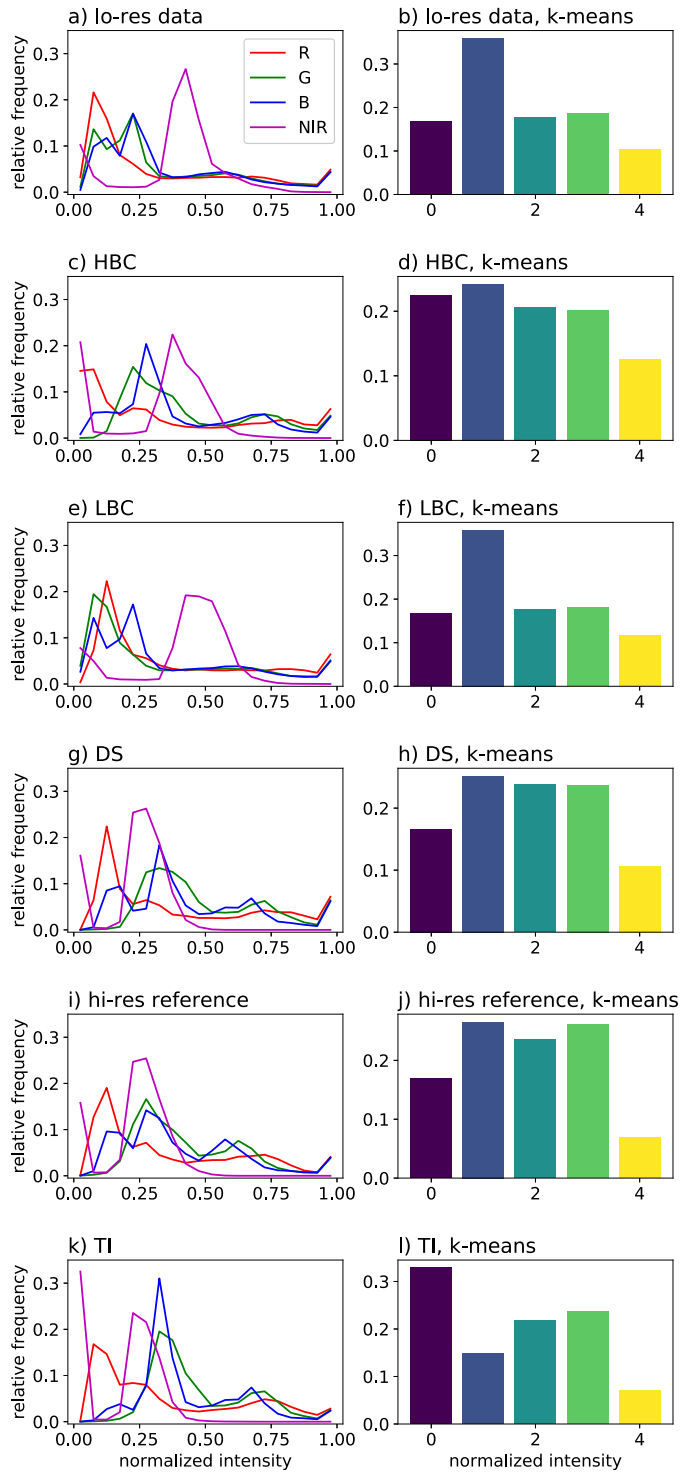


Fig. 11. Histograms for the Port Hedland case study for the R, G, B, and NIR bands and k -means classification. (a) and (b) Lo-res conditioning data. Image downsampled using (c) and (d) HBC, (e) and (f) LBC, and (g) and (h) DS. (i) and (j) Hi-res reference. (k) and (l) TI. The bin colors for the k -means histograms match the class colors in Fig. 9.

with respect to techniques that aim at generating small-scale heterogeneity (see similar results on time series in [45]).

When the chosen TI is not totally compatible with the target image in terms of landscape and intensity histogram, the down-scaled image obtained using DS can present some bias due

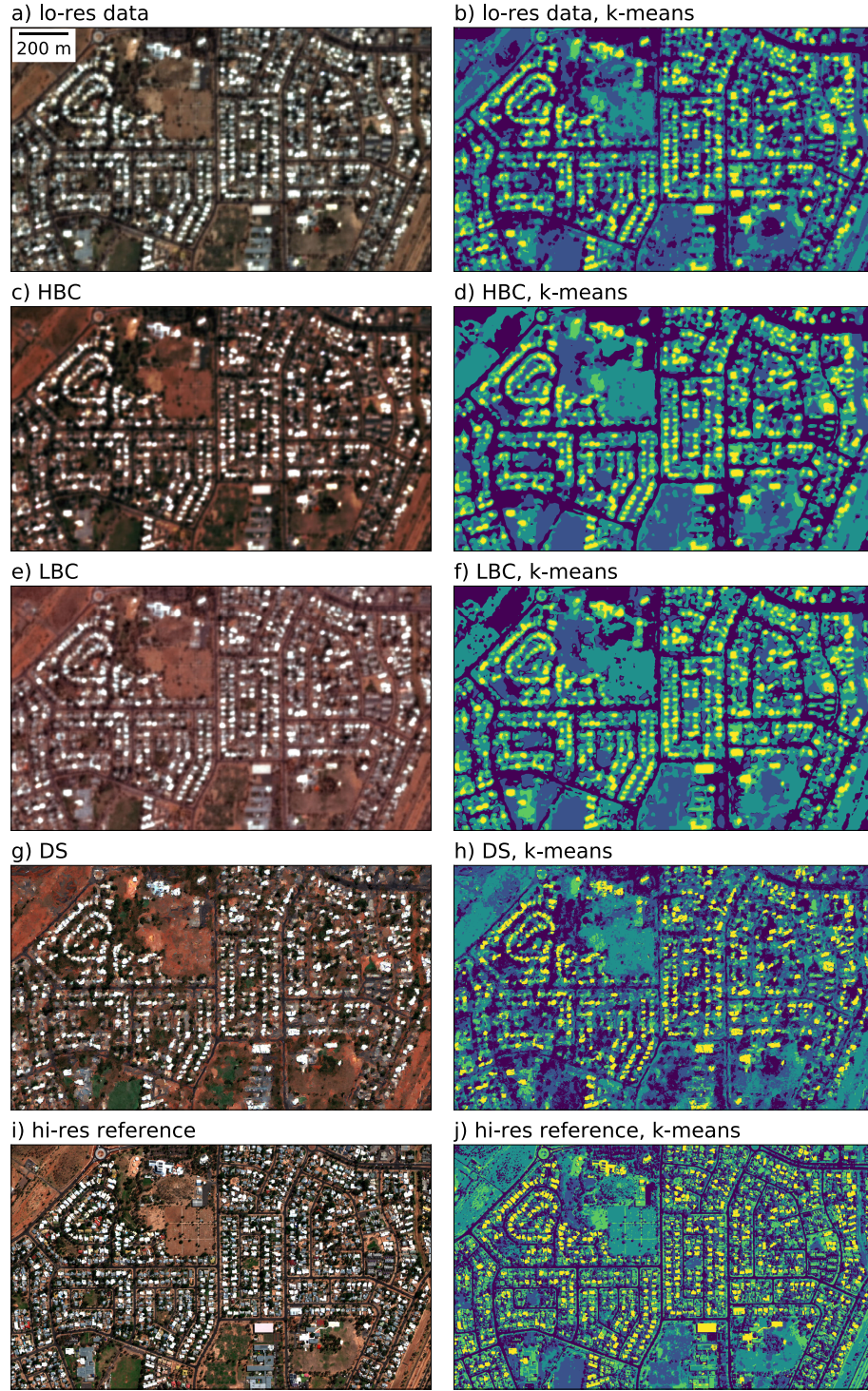


Fig. 12. Visual comparison among RGB images and k -means classification for the Alice Springs-2 case study. (a) and (b) Lo-res input image. Image downsampled using (c) and (d) HBC, (e) and (f) LBC, and (g) and (h) DS. (i) and (j) Reference hi-res image.

to the fact that it embeds the pattern and color information from the TI into the conditioning lo-res structure from the target zone. This is the case of Alice Springs-2 (Section IV-B), where the region chosen as TI, being distant from the target area, presents some different statistical properties, which are reproduced in the downsampled domain of the target zone. However, DS can still recognize and simulate small-scale

patterns (streets and square buildings) that associate the two landscapes, recovering more details than the other techniques considered.

One limitation of the DS technique relates to the preservation of small-scale objects that are unique or do not appear frequently in the TI, e.g., the isolated road in the Botswana case (Fig. 3), the red roof in the detail shown for the Alice

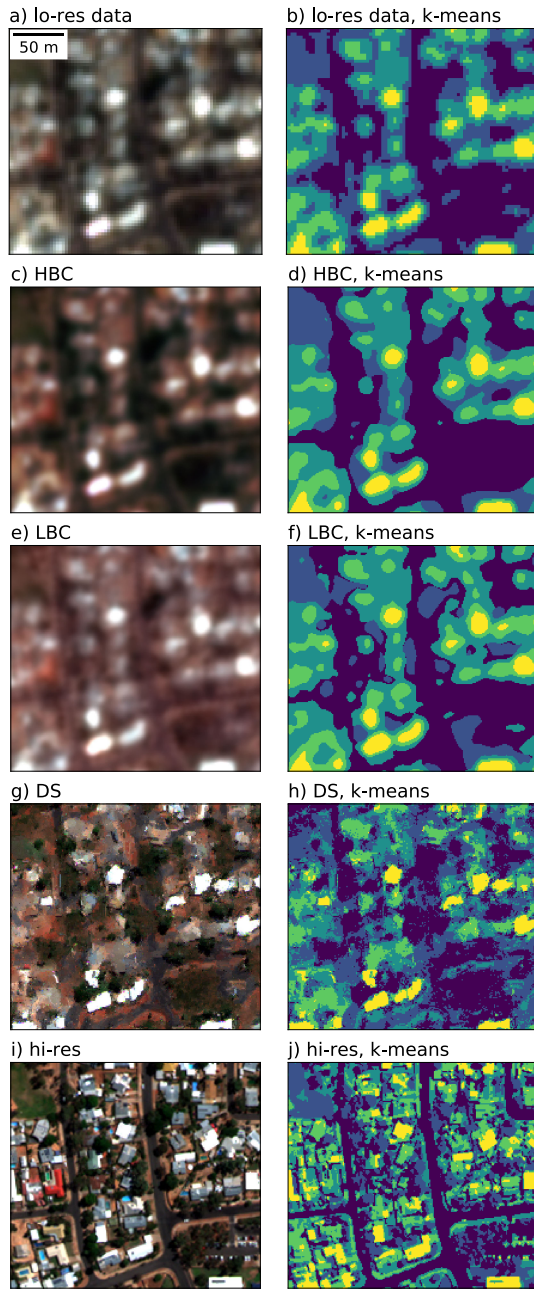


Fig. 13. Details from the Alice Springs-2 case study, showing a visual comparison among RGB images and k -means classification. (a) and (b) Lo-res input image. Image downscaled using (c) and (d) HBC, (e) and (f) LBC, and (g) and (h) DS. (i) and (j) Reference hi-res image.

Springs case (Fig. 7), or the blue-shaded salt deposits on the top of the Port Hedland study region (Fig. 9). Another limitation is the rather poor representation of the fine and continuous structures, e.g., roads [Fig. 6(e)], when these elements are not clearly visible in the lo-res image. Nevertheless, these features are much better reproduced than those with concurrent approaches. While being able to deal with the nonstationary landscapes, the algorithm can better represent natural elements showing a larger repetitiveness in the TI.

The proposed setup can potentially be adapted to specific applications, such as including different auxiliary variables to detect the objects of interest. These can include some

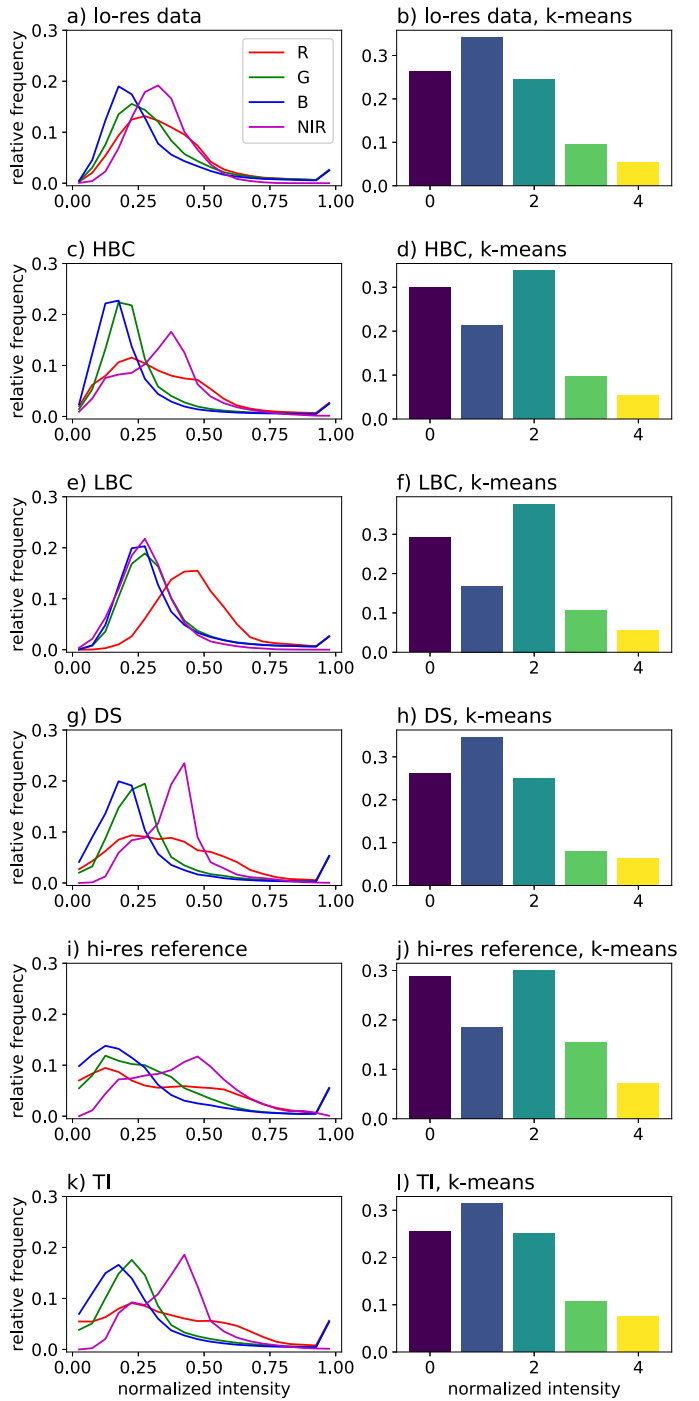


Fig. 14. Histograms for the Alice Springs-2 case study for the R, G, B, and NIR bands and k -means classification. (a) and (b) Lo-res conditioning data. Image downscaled using (c) and (d) HBC, (e) and (f) LBC, and (g) and (h) DS. (i) and (j) Hi-res reference. (k) and (l) TI. The bin colors for the k -means histograms match the class colors in Fig. 12.

commonly available data products, such as the normalized difference vegetation index (NDVI) to provide specific information about vegetation condition, or the thematic maps of road networks, land cover types, and so on. The computational cost of the method is an important consideration and can vary as a function of the target image size and the complexity of the heterogeneity simulated. Indeed, obtaining a downscaled image in the cases presented takes hundreds of CPU-hours (see

TABLE II

QUALITY INDICATORS COMPUTED ON THE DOWNSCALED IMAGES FOR THE TECHNIQUES HBC, LBC, AND DS. THE BEST VALUE (BOLD FONT) TENDS TO 0 FOR ALL INDICATORS, EXCEPTED FOR STRUCTURAL SIMILARITY, WHOSE BEST VALUE TENDS TO 1. CPU TIME IS GIVEN FOR THE DOWNSCALING PROCEDURES, EXCLUDING THE PRELIMINARY IMAGE-REGISTRATION PHASE

	HBC	LBC	DS
Botswana			
RMSE [0,1]	0.242	0.257	0.253
histogram RMSE [pixels]	102.68	238.90	17.10
variogram RMSE [0,1]	0.024	0.029	0.014
structural similarity(SSIM) [-1,1]	0.370	0.356	0.223
k-means miss fraction [0,1]	0.689	0.684	0.715
miss by disagreement [0,1]	0.057	0.021	0.034
miss by location [0,1]	0.632	0.664	0.681
k-means connectivity RMSE [0,1]	0.328	0.345	0.001
CPU time [hours]	< 10 ⁻¹	< 10 ⁻¹	241
Alice Springs			
RMSE [0,1]	0.165	0.176	0.169
histogram RMSE [pixels]	59.21	82.70	31.13
variogram RMSE [0,1]	0.008	0.011	0.005
structural similarity(SSIM) [-1,1]	0.562	0.547	0.508
k-means miss fraction [0,1]	0.504	0.636	0.518
miss by disagreement [0,1]	0.056	0.181	0.061
miss by location [0,1]	0.447	0.455	0.457
k-means connectivity RMSE [0,1]	0.241	0.359	0.092
CPU time [hours]	< 10 ⁻¹	< 10 ⁻¹	61
Port Hedland			
RMSE [0,1]	0.105	0.144	0.093
histogram RMSE [pixels]	420.31	566.57	367.95
variogram RMSE [0,1]	0.009	0.010	0.004
structural similarity(SSIM) [-1,1]	0.721	0.693	0.687
k-means miss fraction [0,1]	0.206	0.231	0.185
miss by disagreement [0,1]	0.120	0.146	0.040
miss by location [0,1]	0.086	0.086	0.145
k-means connectivity RMSE [0,1]	0.086	0.086	0.053
CPU time [hours]	< 10 ⁻¹	< 10 ⁻¹	848
Alice Springs-2			
RMSE [0,1]	0.232	0.235	0.251
histogram RMSE [pixels]	152.139	224.777	132.714
variogram RMSE [0,1]	0.021	0.026	0.011
structural similarity(SSIM) [-1,1]	0.373	0.354	0.300
k-means miss [0,1]	0.595	0.614	0.666
miss by disagreement [0,1]	0.075	0.079	0.160
miss by location [0,1]	0.520	0.535	0.506
k-means connectivity RMSE [0,1]	0.207	0.192	0.081
CPU time [hours]	< 10 ⁻¹	< 10 ⁻¹	1583

Table II), distributable on a multicore cluster. This said, the CPU cost is reasonable when compared with the monetary cost of hi-res acquisitions, or with the unavailability of hi-res acquisitions in the past, which presents a major limit for the change-detection studies. Moreover, it is expected that the next-generation multiple-point algorithms, being developed by several groups in the geostatistical community for other

applications [51]–[54], will be applicable in a similar setting with a reduced computational cost.

The diversity of the study areas used in the tests shows that the proposed technique is adaptive to different types of landscapes without any adjustment to the setup, but with the requirement of a representative TI. A suitable TI can consist of a hi-res image from a nearby region, from the same region but another time step, using the same or another sensor with similar characteristics, or from another region with a similar landscape (e.g., the Alice Springs-2 case). The large-scale structures depicted in the lo-res image should be compatible between the TI and the SG, and possibly repeated in the TI to offer a statistical diversity of the candidate data patterns. To assure this condition, it is a good practice to carefully compare the lo-res images and their histograms and apply a histogram transformation if necessary.

VI. CONCLUSION

In this article, we presented a novel downscaling framework for the multispectral satellite images based on the multiple-point geostatistics. The main rationale is the use of a multivariate TI that contains both hi-res and lo-res imageries, and considered the representative of the heterogeneity being downscaled. Given the lo-res image for the region of interest, the algorithm samples the hi-res data from the TI, where a similar multivariate pattern occurs. In this way, the hi-res image is built without the need of any colocated hi-res data or a complex statistical model. Since the selection of samples is a stochastic process, running the algorithm several times allows generating several equiprobable downscaling realizations, with the potential to estimate uncertainty maps.

The algorithm has been tested on four case studies featuring diverse landscapes, showing good overall performance in generating the realistic hi-res structures related to both natural and man-made features. Although presenting a moderate amount of small-scale noise, the downscaled images compensate for the biases in the intensity histogram of the lo-res image and approximate the shape of the objects in the hi-res reference image. Compared with bicubic interpolation combined with bias correction based on the training data set, the proposed technique shows similar global-error scores, but has the advantage to generate small-scale details and better preserves the intensity histogram. This said, DS is not appropriate to detect the presence of unique or rare types of objects, which are not statistically represented in the training data set.

The proposed workflow can be extended to a variety of remote sensing products in order to balance the tradeoffs in the acquisition properties such as spatial resolution, revisit frequency, footprint area, systematic biases, or commercial cost. This makes the technique attractive for routine scientific and engineering applications. Future research will be devoted to the improvement of the algorithm setup for specific applications, e.g., involving the use of thematic maps or variables derived from the multispectral images. Overall, the approach presents as a promising technique for environmental studies, since it can be used to extend with reasonable approximation expensive hi-res imagery to large areas or simulate the same

image for different time steps to monitor a time-varying process.

REFERENCES

- [1] T. Kemper, M. Jenerowicz, L. Gueguen, D. Poli, and P. Soille, "Monitoring changes in the Menik Farm IDP camps in Sri Lanka using multi-temporal very high-resolution satellite data," *Int. J. Digit. Earth*, vol. 4, no. sup1, pp. 91–106, Nov. 2011.
- [2] A. Rameoelo *et al.*, "Monitoring grass nutrients and biomass as indicators of rangeland quality and quantity using random forest modelling and WorldView-2 data," *Int. J. Appl. Earth Observ. Geoinf.*, vol. 43, pp. 43–54, Dec. 2015.
- [3] K. E. Sawaya, L. G. Olmanson, N. J. Heinert, P. L. Brezonik, and M. E. Bauer, "Extending satellite remote sensing to local scales: Land and water resource monitoring using high-resolution imagery," *Remote Sens. Environ.*, vol. 88, nos. 1–2, pp. 144–156, Nov. 2003.
- [4] D. C. White and M. M. Lewis, "A new approach to monitoring spatial distribution and dynamics of wetlands and associated flows of australian great artesian basin springs using QuickBird satellite imagery," *J. Hydrol.*, vol. 408, nos. 1–2, pp. 140–152, Sep. 2011.
- [5] C. Delacourt, P. Allemand, B. Casson, and H. Vodon, "Velocity field of the 'La Clapière' landslide measured by the correlation of aerial and QuickBird satellite images," *Geophys. Res. Lett.*, vol. 31, no. 15, 2004.
- [6] T. R. Martha *et al.*, "Debris volume estimation and monitoring of Phuktal river landslide-dammed lake in the Zanskar Himalayas, India using Cartosat-2 images," *Landslides*, vol. 14, no. 1, pp. 373–383, Feb. 2017.
- [7] L. K. Grundhauser, "Sentinels rising. Commercial high-resolution satellite imagery and its implications for us national security," Air Univ. Maxwell AFB AI, Airpower J., Maxwell Air Force Base, AB, USA, Accession ADA529857, 1998. [Online]. Available: <https://apps.dtic.mil/sti/citations/ADA529857>
- [8] P. S. Riedel, M. L. Marques, M. V. Ferreira, and M. E. Delaneze, "Proposal of change detection in land cover for pipeline monitoring from rapideye and Ikonos images," *Revista Brasileira de Geofísica*, vol. 32, no. 4, pp. 655–671, 2014.
- [9] J. Gao, *Digital Analysis of Remotely Sensed Imagery*, 1st ed. New York, NY, USA: McGraw-Hill, 2008, ch. 2.4, pp. 48–62.
- [10] R. Houborg and M. McCabe, "High-resolution NDVI from Planet's constellation of Earth observing nano-satellites: A new data source for precision agriculture," *Remote Sens.*, vol. 8, no. 9, p. 768, Sep. 2016.
- [11] M. F. McCabe *et al.*, "The future of Earth observation in hydrology," *Hydrol. Earth Syst. Sci.*, vol. 21, no. 7, pp. 3879–3914, Jul. 2017. [Online]. Available: <https://www.hydrol-earth-syst-sci.net/21/3879/2017/>
- [12] S. Kolios, G. Georgoulas, and C. Stylios, "Achieving downscaling of meteosat thermal infrared imagery using artificial neural networks," *Int. J. Remote Sens.*, vol. 34, no. 21, pp. 7706–7722, Nov. 2013.
- [13] C. Lanaras, E. Baltsavias, and K. Schindler, "Hyperspectral super-resolution with spectral unmixing constraints," *Remote Sens.*, vol. 9, no. 11, p. 1196, Nov. 2017.
- [14] Q. Wang *et al.*, "Fusion of landsat 8 OLI and sentinel-2 MSI data," *IEEE Trans. Geosci. Remote Sens.*, vol. 55, no. 7, pp. 3885–3899, Jul. 2017.
- [15] C. Lanaras, J. Bioucas-Dias, S. Galliani, E. Baltsavias, and K. Schindler, "Super-resolution of Sentinel-2 images: Learning a globally applicable deep neural network," 2018, *arXiv:1803.04271*. [Online]. Available: <http://arxiv.org/abs/1803.04271>
- [16] P. M. Atkinson, E. Pardo-Iguzquiza, and M. Chica-Olmo, "Downscaling cokriging for super-resolution mapping of continua in remotely sensed images," *IEEE Trans. Geosci. Remote Sens.*, vol. 46, no. 2, pp. 573–580, Feb. 2008.
- [17] Y. Tang, P. M. Atkinson, and J. Zhang, "Downscaling remotely sensed imagery using area-to-point cokriging and multiple-point geostatistical simulation," *ISPRS J. Photogramm. Remote Sens.*, vol. 101, pp. 174–185, Mar. 2015.
- [18] Q. Wang, W. Shi, P. M. Atkinson, and Y. Zhao, "Downscaling MODIS images with area-to-point regression kriging," *Remote Sens. Environ.*, vol. 166, pp. 191–204, Sep. 2015.
- [19] X. Li, L. Wang, Q. Cheng, P. Wu, W. Gan, and L. Fang, "Cloud removal in remote sensing images using nonnegative matrix factorization and error correction," *ISPRS J. Photogramm. Remote Sens.*, vol. 148, pp. 103–113, Feb. 2019.
- [20] K. Zhang, Q. Liu, H. Song, and X. Li, "A variational approach to simultaneous image segmentation and bias correction," *IEEE Trans. Cybern.*, vol. 45, no. 8, pp. 1426–1437, Aug. 2015.
- [21] S. Mukherjee, P. K. Joshi, and R. D. Garg, "Regression-kriging technique to downscale satellite-derived land surface temperature in heterogeneous agricultural landscape," *IEEE J. Sel. Topics Appl. Earth Observ. Remote Sens.*, vol. 8, no. 3, pp. 1245–1250, Mar. 2015.
- [22] W. P. Kustas, J. M. Norman, M. C. Anderson, and A. N. French, "Estimating subpixel surface temperatures and energy fluxes from the vegetation index–radiometric temperature relationship," *Remote Sens. Environ.*, vol. 85, no. 4, pp. 429–440, Jun. 2003.
- [23] N. Agam, W. P. Kustas, M. C. Anderson, F. Li, and C. M. U. Neale, "A vegetation index based technique for spatial sharpening of thermal imagery," *Remote Sens. Environ.*, vol. 107, no. 4, pp. 545–558, Apr. 2007.
- [24] W. Ha, P. H. Gowda, and T. A. Howell, "Downscaling of land surface temperature maps in the Texas high plains with the TsHARP method," *GISci. Remote Sens.*, vol. 48, no. 4, pp. 583–599, Oct. 2011.
- [25] S. Bonafoni, "Downscaling of landsat and MODIS land surface temperature over the heterogeneous urban area of Milan," *IEEE J. Sel. Topics Appl. Earth Observ. Remote Sens.*, vol. 9, no. 5, pp. 2019–2027, May 2016.
- [26] M. Stathopoulou and C. Cartalis, "Downscaling AVHRR land surface temperatures for improved surface urban heat island intensity estimation," *Remote Sens. Environ.*, vol. 113, no. 12, pp. 2592–2605, Dec. 2009.
- [27] M. Mahmud, M. Hashim, H. Matsuyama, S. Numata, and T. Hosaka, "Spatial downscaling of satellite precipitation data in humid tropics using a site-specific seasonal coefficient," *Water*, vol. 10, no. 4, p. 409, Mar. 2018.
- [28] Y. Kim and N.-W. Park, "Comparison of regression models for spatial downscaling of coarse scale satellite-based precipitation products," in *Proc. IEEE Int. Geosci. Remote Sens. Symp. (IGARSS)*, Jul. 2017, pp. 4634–4637.
- [29] C. Zhan, J. Han, S. Hu, L. Liu, and Y. Dong, "Spatial downscaling of GPM annual and monthly precipitation using regression-based algorithms in a mountainous area," *Adv. Meteorol.*, vol. 2018, 2018, Art. no. 1506017, doi: [10.1155/2018/1506017](https://doi.org/10.1155/2018/1506017).
- [30] M. Piles *et al.*, "Downscaling SMOS-derived soil moisture using MODIS visible/infrared data," *IEEE Trans. Geosci. Remote Sens.*, vol. 49, no. 9, pp. 3156–3166, Sep. 2011.
- [31] M. Piles *et al.*, "A downscaling approach for SMOS land observations: Evaluation of high-resolution soil moisture maps over the Iberian Peninsula," *IEEE J. Sel. Topics Appl. Earth Observ. Remote Sens.*, vol. 7, no. 9, pp. 3845–3857, Sep. 2014.
- [32] Y. Jin, Y. Ge, J. Wang, and G. B. M. Heuvelink, "Deriving temporally continuous soil moisture estimations at fine resolution by downscaling remotely sensed product," *Int. J. Appl. Earth Observ. Geoinf.*, vol. 68, pp. 8–19, Jun. 2018.
- [33] A. Zhong *et al.*, "Downscaling of passive microwave soil moisture retrievals based on spectral analysis," *Int. J. Remote Sens.*, vol. 39, no. 1, pp. 50–67, Jan. 2018.
- [34] P. K. Srivastava, D. Han, M. R. Ramirez, and T. Islam, "Machine learning techniques for downscaling SMOS satellite soil moisture using MODIS land surface temperature for hydrological application," *Water Resour. Manage.*, vol. 27, no. 8, pp. 3127–3144, Jun. 2013.
- [35] D. D. Alexakis and I. K. Tsanis, "Comparison of multiple linear regression and artificial neural network models for downscaling TRMM precipitation products using MODIS data," *Environ. Earth Sci.*, vol. 75, no. 14, Jul. 2016.
- [36] W. Jing, Y. Yang, X. Yue, and X. Zhao, "A spatial downscaling algorithm for satellite-based precipitation over the tibetan plateau based on NDVI, DEM, and land surface temperature," *Remote Sens.*, vol. 8, no. 8, p. 655, Aug. 2016.
- [37] G. Mariethoz, P. Renard, and J. Straubhaar, "The direct sampling method to perform multiple-point geostatistical simulations," *Water Resour. Res.*, vol. 46, p. W11536, Nov. 2010.
- [38] G. Yin, G. Mariethoz, and M. McCabe, "Gap-filling of landsat 7 imagery using the direct sampling method," *Remote Sens.*, vol. 9, no. 1, p. 12, Dec. 2016.
- [39] F. Oriani *et al.*, "Simulating small-scale rainfall fields conditioned by weather state and elevation: A data-driven approach based on rainfall radar images," *Water Resour. Res.*, vol. 53, no. 10, pp. 8512–8532, Oct. 2017. [Online]. Available: <https://agupubs.onlinelibrary.wiley.com/doi/abs/10.1002/2017WR020876>
- [40] S. K. Jha, G. Mariethoz, J. Evans, M. F. McCabe, and A. Sharma, "A space and time scale-dependent nonlinear geostatistical approach for downscaling daily precipitation and temperature," *Water Resour. Res.*, vol. 51, no. 8, pp. 6244–6261, Aug. 2015, doi: [10.1002/2014WR016729](https://doi.org/10.1002/2014WR016729).

- [41] F. Guardiano and R. Srivastava, "Multivariate geostatistics: Beyond bivariate moments," *Geostatistics Tróia*, vol. 1. Dordrecht, The Netherlands: Springer, 1993, pp. 133–144.
- [42] S. Strebelle, "Conditional simulation of complex geological structures using multiple-point statistics," *Math. Geol.*, vol. 34, no. 1, pp. 1–21, Jan. 2002.
- [43] E. Meerschman, G. Pirot, G. Mariethoz, J. Straubhaar, M. Van Meirvenne, and P. Renard, "A practical guide to performing multiple-point statistical simulations with the direct sampling algorithm," *Comput. Geosci.*, vol. 52, pp. 307–324, Mar. 2013.
- [44] F. Oriani, J. Straubhaar, P. Renard, and G. Mariethoz, "Simulation of rainfall time series from different climatic regions using the direct sampling technique," *Hydrol. Earth Syst. Sci.*, vol. 18, pp. 3015–3031, 2014.
- [45] F. Oriani, A. Borghi, J. Straubhaar, G. Mariethoz, and P. Renard, "Missing data simulation inside flow rate time-series using multiple-point statistics," *Environ. Model. Softw.*, vol. 86, pp. 264–276, Dec. 2016.
- [46] S. Lloyd, "Least squares quantization in PCM," *IEEE Trans. Inf. Theory*, vol. IT-28, no. 2, pp. 129–137, Mar. 1982.
- [47] R. Houborg and M. McCabe, "Daily retrieval of NDVI and LAI at 3 m resolution via the fusion of CubeSat, landsat, and MODIS data," *Remote Sens.*, vol. 10, no. 6, p. 890, Jun. 2018.
- [48] H. Hou and H. Andrews, "Cubic splines for image interpolation and digital filtering," *IEEE Trans. Acoust., Speech, Signal Process.*, vol. ASSP-26, no. 6, pp. 508–517, Dec. 1978.
- [49] S. Wang, "Application of self-organising maps for data mining with incomplete data sets," *Neural Comput. Appl.*, vol. 12, no. 1, pp. 42–48, Sep. 2003.
- [50] J. M. Hovadik and D. K. Larue, "Static characterizations of reservoirs: Refining the concepts of connectivity and continuity," *Petroleum Geosci.*, vol. 13, no. 3, pp. 195–211, Aug. 2007.
- [51] K. Mahmud, G. Mariethoz, J. Caers, P. Tahmasebi, and A. Baker, "Simulation of Earth textures by conditional image quilting," *Water Resour. Res.*, vol. 50, no. 4, pp. 3088–3107, Apr. 2014.
- [52] E. Laloy, R. Héroult, J. Lee, D. Jacques, and N. Linde, "Inversion using a new low-dimensional representation of complex binary geological media based on a deep neural network," *Adv. Water Resour.*, vol. 110, pp. 387–405, Dec. 2017.
- [53] M. Pourfard, M. J. Abdollahifard, K. Faez, S. A. Motamedi, and T. Hosseiniyan, "PCTO-SIM: Multiple-point geostatistical modeling using parallel conditional texture optimization," *Comput. Geosci.*, vol. 102, pp. 116–138, May 2017.
- [54] M. Gravey, L. G. Rasera, and G. Mariethoz, "Analogue-based colorization of remote sensing images using textural information," *ISPRS J. Photogramm. Remote Sens.*, vol. 147, pp. 242–254, Jan. 2019.



Fabio Oriani received the Ph.D. degree from the University of Neuchâtel, Neuchâtel, Switzerland, in 2015. He collaborated with developers and practitioners at different research institutes, including the Water Research Center (WRC, Sydney) and the Geological Survey of Denmark and Greenland (GEUS, Copenhagen). He is a Research Assistant with the Geostatistical Algorithms and Image Analysis Lab, University of Lausanne, Lausanne, Switzerland. His research interests include the development of stochastic techniques for the simulation and analysis of remote sensing and hydroclimate data.



Matthew F. McCabe received the Ph.D. degree in civil and environmental engineering from the University of Newcastle, Newcastle, Australia, in 2003.

He worked as a Post-Doctoral Researcher with the Princeton University, Princeton, NJ, USA, and Los Alamos National Laboratory, Los Alamos, NM, USA, before taking up a faculty position at the University of New South Wales, Sydney, Australia, in 2008. He is a Professor of remote sensing and water security with the King Abdullah University of Science and Technology, Thuwal, Saudi Arabia, where he leads the Hydrology, Agriculture and Land Observation Laboratory. His research interests encompass a broad range of topics related to water and food security, climate change impacts, precision agriculture, water resources monitoring and modeling, and the novel use of technologies for enhanced Earth system observation. He has published over 200 research contributions and has been recognized as a Clarivate Highly Cited Researcher.

where he leads the Hydrology, Agriculture and Land Observation Laboratory. His research interests encompass a broad range of topics related to water and food security, climate change impacts, precision agriculture, water resources monitoring and modeling, and the novel use of technologies for enhanced Earth system observation. He has published over 200 research contributions and has been recognized as a Clarivate Highly Cited Researcher.



Gregoire Mariethoz received the M.S., M.A.S., and Ph.D. degrees from the University of Neuchâtel, Neuchâtel, Switzerland, in 2003, 2006, and 2009, respectively.

Between 2009 and 2010, he was a Post-Doctoral Researcher with Stanford University, Stanford, CA, USA, and between 2010 and 2014, he was a Senior Lecturer with the University of New South Wales, Sydney, NSW, Australia. Since 2014, he has been a Professor with the University of Lausanne, Lausanne, Switzerland. His research interests include the development of spatial statistics algorithms and their application in earth surface observation, hydrology, and hydrogeology.